Composition-Dependent Crystallization Behavior of Molybdate and Oxyapatite in High-Level Waste Glass

ZHANG, Lejian, JIA, Ziqiang, FENG, Jinyang, DENG, Wei, OJOVAN, Michael I <http://orcid.org/0000-0001-8928-4879> and XU, Kai <http://orcid.org/0000-0001-8212-0337>

Composition-Dependent Crystallization Behavior of Molybdate and Oxyapatite in High-Level Waste Glass

Lejian Zhang[a], Ziqiang Jia[a], Jinyang Feng[a], Wei Deng[b], Michael I. Ojovan[a], Kai Xu[a,*]

[a] State Key Laboratory of Silicate Materials for Architectures, Wuhan University of Technology, 430070, Wuhan, China

[b] School of Engineering and Built Environment, College of Business, Technology and Engineering, Sheffield Hallam University, City Campus, Howard Street, Sheffield, S1 1WB, UK.

[*] Corresponding author

E-mail address: kaixu@whut.edu.cn (K. Xu)

`

Abstract

Borosilicate glass, widely used as a host matrix for high-level radioactive waste (HLW) vitrification, encounters substantial difficulties when incorporating waste streams containing elevated levels of molybdenum and rare-earth elements. This challenge arises because molybdenum and rare-earth species, frequently present in HLW compositions, possess a pronounced tendency to initiate crystallization processes. Such crystallization not only causes deviations in the final glass properties from the desired design specifications but also threatens the operational reliability of the glass-melting system. Although the crystallization behavior of glass during vitrification is known to be critically dependent on its composition, a systematic investigation into this relationship remains notably absent. Herein, by designing and characterizing addressing this dependence remains limited. In the present work, simulated waste glasses with controlled variations in alkaline earth oxide, B_2O_3, MoO_3, and rare-earth oxide concentrations were prepared and analyzed to examine the role of composition in governing crystallization behavior. Our results reveal the competitive crystallization of two primary phases within the simulated glass systems, namely calcium molybdate ($CaMoO_4$) and oxyapatite ($Ca_2Ln_8(SiO_4)_6O_2$, where Ln denotes lanthanide elements). This competition is composition-dependent; in particular, higher levels of B_2O_3 and MoO_3 markedly enhance the precipitation of $CaMoO_4$ while inhibiting oxyapatite. Conversely, enriching the glass with alkaline earth and rare-earth oxides promote the development of the oxyapatite phase. This observed competitive crystallization mechanism establishes a theoretical framework for tailoring glass crystallization behavior through compositional design of the base glass.

Keywords:

Nuclear Waste, Vitrification, High-Level Radioactive Waste, Crystallization, Calcium Molybdate, Oxyapatite

`

1. Introduction

Borosilicate glass is considered the standard immobilization medium for high-level radioactive waste (HLW) vitrification, mainly due to its adaptable network structure and outstanding chemical durability, which facilitate incorporation of a wide range of elements within a stable matrix [1-4]. Nevertheless, several limitations remain under practical processing conditions. The performance and melt-processing characteristics of borosilicate glass are significantly restricted by its limited tolerance toward certain anionic species, especially molybdate and sulfate [4–8]. These large anions with low field strength function as network modifiers instead of network formers and may interrupt the integrity of the borosilicate network, resulting in segregation with charge-balancing alkali or alkaline earth cations and eventual crystallization as molybdate-containing phases [9]. Owing to the considerable chemical stability of calcium molybdate ($CaMoO_4$), its precipitation is considered an effective strategy for molybdenum immobilization [10]. Consequently, a common strategy is to incorporate alkaline earth metals into the glass network, promoting the formation of a chemically stable glass-ceramic composite [11] where Mo is immobilized within the stable $CaMoO_4$ crystalline phase [12].

However, the relatively high density of $CaMoO_4$ introduces significant operational challenges in Joule-heated ceramic melters. During extended melting or idling periods, accumulation of this phase at the base of the melter may occur, leading to serious refractory corrosion and possible electrical short-circuiting between bottom electrodes [13]. Furthermore, rare-earth metal oxides, which behave as network modifiers and exhibit limited solubility in the glass matrix, can readily induce crystallization of the structurally compatible oxyapatite phase ($Ca_2Ln_8(SiO_4)_6O_2$, where Ln represents lanthanide elements), thereby causing pronounced compositional segregation [14–17] when the rare-earth element (RE) content is high.

Within nuclear waste vitrification processes, the overall composition of HLW depends on the fuel rod configuration, burn-up level, and subsequent reprocessing procedures. For instance, the MoO_3 content may range from about 2.0 wt% to values exceeding 4.5 wt%, whereas rare-earth oxide concentrations in HLW glasses typically lie between 4.5 wt% and 9.0 wt% for burn-up levels of 30–45 GW·d/t·U [18]. Notably, the composition of alkaline earth metal oxides varies between MgO-rich Atelier de

`

Vitrification Marcoule (AVM) glasses and CaO-containing R7T7 glasses, largely due to differences associated with reactor type (e.g., light-water versus gas-graphite reactors). Moreover, glass melting operations can introduce compositional fluctuations. For instance, nearly 15% of B_2O_3 may volatilize from the melt at 1100 °C over 96 h in the absence of a cold cap [19]. Therefore, it is imperative to investigate effects of compositional variations on crystallization behavior of molybdate and oxyapatite in nuclear waste glass.

Accordingly, the present study systematically designed a set of simulated HLW glass compositions to explore the influence of molybdenum oxide, rare-earth oxides (originating from the simulated waste stream), as well as boron oxide and alkaline earth oxides (introduced for compositional optimization), on the crystallization behavior of molybdate and oxyapatite phases. Investigation of the individual contributions of these components to crystallization behavior provides theoretical guidance for compositional optimization and process control in industrial HLW glass production.

2. Experimental

2.1. Preparation of Simulated HLW Glasses

The centroid glass (CG) composition was selected as a representative simulated HLW glass for immobilization of waste derived from commercial reprocessing facilities. By varying the content of a single component while keeping the ratios of all other constituent's constant based on the CG glass composition, four distinct series of simplified glasses were designed as shown in Table 1. The molybdenum oxide and rare-earth oxide series were designed to emulate variations in waste stream composition, whereas the boron oxide and alkaline earth oxide series were established for compositional refinement.

Of precursor materials, 100 g was thoroughly blended using a planetary ball mill for 2 h. All reagents (analytical grade) were obtained from Sinopharm Chemical Reagent Co., Ltd. The homogenized mixtures were subsequently transferred into covered alumina crucibles (150 mL) and melted in a muffle furnace at 1150 °C for 2 h. The molten glasses were then poured into graphite molds and annealed at 450 °C for 4 h to alleviate residual thermal stress.

`

The prepared glass samples underwent non-isothermal heat treatment. In this process, the samples were placed in alumina crucibles (30 mL) and heated in air atmosphere from ambient temperature to 700, 750, 800, 850, and 900 °C at a heating rate of 10 °C/min, followed by a holding duration of 120 h.

2.2. Characterization of Samples

Thermal characteristics of the samples were evaluated using differential scanning calorimetry (DSC, NETZSCH STA449 F3). Finely powdered glass specimens were tested under an argon atmosphere within the temperature range of 200–1200 °C at a heating rate of 20 °C/min.

Crystalline phase identification of the heat-treated glasses was performed using X-ray diffraction (XRD, Bruker D8 DISCOVER). Measurements were conducted at 40 kV and 40 mA employing Cu Kα radiation with a step size of 0.02 °/s over a 2θ range of 15°–65°. The degree of crystallinity was estimated semi-quantitatively through Rietveld refinement using JADE 6.0 software.

Microstructural morphology of the samples was examined using scanning electron microscopy (SEM, Zeiss Ultra Plus). Elemental compositions of the precipitated phases were analyzed by energy-dispersive X-ray spectroscopy (EDS, Oxford X-max 50). For specimen preparation, bulk samples were embedded in epoxy resin, followed by successive grinding and polishing steps.

Structural modifications in the glass samples after various heat treatments were further investigated using a laser confocal micro-Raman spectrometer (LabRAM HR Evolution). Raman spectra were recorded with a 532 nm excitation laser, an acquisition time of 10 s, 10 accumulations, and within a spectral range of 200–1400 cm^{-1}.

3. Results and Discussion

3.1. Thermal Analysis of Glasses

To improve the clarity of characteristic thermal transitions and enable precise identification, first-derivative DSC (DDSC) profiles were generated through numerical differentiation of the original DSC data, as illustrated in Fig. S1. On the basis of these DDSC curves, the crystallization peak temperature was extracted.

`

The crystallization peak temperature exhibited a pronounced dependence on the glass composition. Fig. 1 plots the crystallization peak temperature (T_p) as a function of composition for samples displaying a clear exothermic signal in DSC analysis. In the CG sample, the crystallization peak temperature was observed at 750 °C. For the Mo series, the crystallization peak temperatures of samples Mo3 and Mo4, obtained from DDSC analysis, were determined to be 680 °C and 610 °C, respectively. The reduction in crystallization peak temperature with increasing MoO_3 concentration is related to the limited solubility of molybdenum in borosilicate glass melts [20]. Moreover, the precipitated molybdate can act as heterogeneous nucleation sites, thereby reducing the activation energy for glass crystallization. [20].

Within the boron oxide series, the crystallization peak temperature of samples B10, B20, and B25 were measured as 770 °C, 730 °C, and 700 °C, respectively. The crystallization peak temperature gradually shifts toward lower values with increasing B_2O_3 concentration. In the rare-earth oxide series, the crystallization onset temperatures for RE9 and RE12 were both found to be 800 °C, suggesting that the crystallization temperature remained largely unchanged with increasing rare-earth oxide content. In contrast, for the alkaline earth oxide series, no distinct crystallization peaks were detected in the DDSC curves of samples AE5 and AE15.

3.2. Calculation of Crystallinity in Heat-Treated Samples

The crystallinity of the prepared glass samples was evaluated and mutually validated using two complementary approaches. The first approach was based on DSC analysis. The crystallization fraction (X) was calculated according to the following formula [21]:

$$X=\frac{A_i}{A} \quad (1)$$

where X represents the crystallization fraction of the sample, A represents the total area of the exothermic peak between the crystallization onset ($T_{p,onset}$) and end ($T_{p,end}$) temperatures, and A_i corresponds to the partial peak area between T_p and a selected heat-treatment temperature (T_i).

The second approach involved analysis of XRD data. Crystallinity values were calculated using the Rietveld refinement method for semi-quantitative analysis implemented in JADE 6.0 software [14]. It should be emphasized that the obtained

`

values indicate comparative semi-quantitative trends rather than exact crystalline fractions. The crystallization peak temperature (T_p) was determined to be 750 °C, and the crystallization process was completed at about 840 °C (Fig. S2a). Only diffraction peaks associated with the calcium molybdate phase ($CaMoO_4$, PDF #85–0546) from the sample treated at 850 °C are presented in Fig. S2b. Figure 2 shows the relationship between the crystallization fraction calculated by DSC and the crystallinity of the CG sample obtained by XRD as a function of heat-treatment temperature. The DSC-derived crystallization fraction curve indicates that the crystallization behavior of the CG sample essentially finishes at around 840 °C, reaching the maximum crystallized amount. XRD semi-quantitative calculation results demonstrate that the CG sample attains a maximum crystallinity of nearly 1% at 850 °C. The agreement between crystallization tendency derived from DSC and XRD analyses verifies the reliability of the applied evaluation methods.

3.3. XRD Analysis of Samples Heat-Treated at 800 °C

XRD characterization was carried out on glass samples subjected to heat treatment at 800 °C for 120 h. Fig. 3a shows the XRD patterns of glass samples containing different levels of alkaline earth oxides. As the AE content in the CG glass increases, distinct crystalline diffraction peaks become evident in sample AE15. These reflections were indexed to the $Ca_2Ln_8(SiO_4)_6O_2$ phase (PDF #78–1038).

Fig. 3b presents the XRD patterns of glass samples with varying B_2O_3 content. Samples B5 and B10 display diffraction peaks attributable to the $Ca_2Ln_8(SiO_4)_6O_2$ phase. The intensity of these peaks progressively decreases and eventually disappears with increasing B_2O_3 content. Upon further increase in B_2O_3 concentration, samples B20 and B25 exhibit the emergence of diffraction peaks corresponding to the $CaMoO_4$ phase, with the peak intensity increasing at higher B_2O_3 levels.

Fig. 3c illustrates the XRD patterns of glass samples with different molybdenum oxide contents. Samples Mo0 and Mo1 exhibit diffraction peaks associated with the $Ca_2Ln_8(SiO_4)_6O_2$ phase. The intensity of these peaks gradually weakens and ultimately vanishes with increasing MoO_3 concentration. With further addition of molybdenum oxide, samples Mo3 and Mo4 demonstrate the formation of the $CaMoO_4$ phase, accompanied by an increase in peak intensity as MoO_3 content rises.

`

Fig. 3d shows the XRD patterns of the glass series containing different rare-earth oxide contents. Samples RE0 and RE3 present diffraction peaks of the $CaMoO_4$ phase. The intensity of these peaks progressively decreases and eventually disappears with increasing RE content. As the RE content is further increased, samples RE9 and RE12 display the appearance of diffraction peaks corresponding to the $Ca_2Ln_8(SiO_4)_6O_2$ phase, with increasing peak intensity at higher RE concentrations.

Fig. 4 displays a spider plot representing the variation in crystallinity with composition for glass samples treated at 800 °C for 120 h. The molybdenum oxide series is marked in red, the rare-earth oxide series in grey, the boron oxide series in blue, and the alkaline earth oxide series in green. Solid guide lines indicate the trend in crystallinity of $CaMoO_4$ with changing composition, while dashed guide lines indicate the trend for $Ca_2Ln_8(SiO_4)_6O_2$ crystallinity. The CG sample is located at the center of the plot, reflecting its predominantly amorphous nature. Modifications in the CG composition lead to precipitation of either $CaMoO_4$ or $Ca_2Ln_8(SiO_4)_6O_2$ phases following heat treatment. The crystallization fraction of $CaMoO_4$ ranges from 0% to 30%, whereas that of $Ca_2Ln_8(SiO_4)_6O_2$ varies between 0% and 15%. A competitive precipitation relationship between these two crystalline phases can be observed:

(1) Effect of AE/RE: Increasing the alkaline earth oxide content from 6.4 wt% to 10.3 wt% enhances the $Ca_2Ln_8(SiO_4)_6O_2$ crystallinity from 0% to 5%. As the rare-earth oxide content increases from 0 wt% to 7.0 wt%, the crystallinity of $CaMoO_4$ decreases from 2% to 0%. Further increasing the rare-earth oxide content to 13.7 wt% promotes $Ca_2Ln_8(SiO_4)_6O_2$ crystallinity from 0% to 15%, while completely inhibiting $CaMoO_4$ formation.

(2) Effect of MoO_3/B_2O_3: Increasing the molybdenum oxide content from 0 wt% to 2.0 wt% causes the $Ca_2Ln_8(SiO_4)_6O_2$ crystallinity to drop from 3% to 0%. When the molybdenum oxide content is increased to 4.6 wt%, $CaMoO_4$ precipitation is triggered, with its crystallinity jumping to 30%. Similarly, increasing the boron oxide content from 5.8 wt% to 14.4 wt% reduces the $Ca_2Ln_8(SiO_4)_6O_2$ crystallinity from 15% to zero. A further increase to 28.1 wt% triggers $CaMoO_4$ precipitation, yielding a crystallinity of about 5%.

`

In summary, increasing the content of alkaline earth or rare-earth oxides facilitates precipitation of $Ca_2Ln_8(SiO_4)_6O_2$ while simultaneously suppressing the $CaMoO_4$ formation. Conversely, an increase in molybdenum oxide or boron oxide results in the opposite trend.

3.4. XRD Analysis of Samples Heat-Treated at Different Temperatures

Fig. 5 presents the XRD patterns of selected glass samples after heat treatment within the temperature range of 700 °C to 900 °C for 120 h. Fig. 5a illustrates the XRD patterns of the Mo0 glass sample. A diffraction peak corresponding to the $Ca_2Ln_8(SiO_4)_6O_2$ phase is detected only in the specimen treated at 800 °C, whereas no evident crystalline peaks are observed at the other temperatures. Fig. 5b shows the XRD patterns of the Mo4 glass sample. The $CaMoO_4$ phase is present in all samples subjected to heat treatment between 700 °C and 900 °C. The intensity of its diffraction peaks gradually declines as the heat-treatment temperature increases. Fig. 5c depicts the XRD patterns of the RE0 glass sample. The $CaMoO_4$ phase is identified in samples treated from 700 °C to 850 °C. The peak intensity rises with increasing temperature, reaching a maximum at 750 °C, and subsequently decreases with further heating. The crystalline phase completely dissolves at 900 °C, as evidenced by the disappearance of diffraction peaks. Fig. 5d presents the XRD patterns of the RE12 glass sample. Diffraction peaks indexed to the $Ca_2Ln_8(SiO_4)_6O_2$ phase initially appear at 750 °C. The peak intensity increases with temperature, attaining a maximum at 850 °C, followed by a reduction at 900 °C.

Fig. 6 illustrates the variation in crystallinity as a function of temperature for glass samples containing high MoO_3 content, low MoO_3 content, high RE content, low RE content, and the CG composition. As shown in Fig. 6a, in the glass with elevated molybdenum oxide content, the crystallinity of the precipitated $CaMoO_4$ phase decreases continuously as the heat-treatment temperature increases from 700 °C to 900 °C. Compared with the CG sample, which exhibits maximum crystallinity at 850 °C in Fig. 2, the glass with high Mo content shows a markedly lower temperature corresponding to maximum crystallinity, consistent with the DSC results. Fig. 6b presents the crystallinity of glasses with reduced molybdenum oxide content. When the Mo concentration is lowered, the precipitated phase becomes $Ca_2Ln_8(SiO_4)_6O_2$. The crystallinity of this phase initially increases and subsequently decreases across the

`

temperature range of 700–900 °C. Both Mo0 and Mo1 samples attain their peak crystallinity at about 800 °C. Fig. 6c displays the crystallinity of glass containing a high rare-earth content. Under this composition, only the $Ca_2Ln_8(SiO_4)_6O_2$ phase precipitates. Its crystallinity exhibits a similar trend of initial increase followed by decline between 700 °C and 900 °C, with the maximum crystallinity observed around 850 °C. Fig. 6d shows the crystallinity of glasses with low RE content in comparison with the CG sample. For compositions with reduced RE content, only the $CaMoO_4$ phase precipitates. Likewise, the crystallinity increases initially and then decreases within the 700–900 °C temperature range. Furthermore, a decrease in rare-earth oxide content leads to a reduction in the temperature at which maximum crystallinity occurs.

3.5. SEM and EDS Analysis of the Precipitated Crystals

Fig. 7 presents the microstructures of B5 and RE12 glass samples after heat treatment at 800 °C for 120 h followed by hydrofluoric acid (HF) etching. Field emission scanning electron microscopy (FE-SEM) combined with energy-dispersive spectroscopy (EDS) elemental mapping was employed for characterization. Fig. 7a shows that the B5 glass matrix precipitates a crystalline phase exhibiting a horn-like or bifurcated dendritic morphology, with an approximate length of 70 μm. The corresponding EDS elemental maps reveal that the precipitate is enriched in Ca, La, Ce, and Nd, whereas the Si signal is relatively weak. This compositional result agrees with the XRD analysis (Fig. 3b), confirming that the precipitated phase corresponds to the oxyapatite-structured crystal $Ca_2Ln_8(SiO_4)_6O_2$. Fig. 7b displays the RE12 sample, in which the rare-earth oxide content was increased to 13.66 wt%. After undergoing the same heat treatment at 800 °C for 120 h, a dendritic crystal phase with morphology similar to that observed in the B5 glass precipitated within the sample. EDS analysis of this region also detects characteristic signals of Ca, La, Ce, and Nd, verifying that the precipitated phase is $Ca_2Ln_8(SiO_4)_6O_2$, consistent with the XRD results of this sample (Fig. 3d). These findings indicate that, despite compositional differences between the two glass series, the same $Ca_2Ln_8(SiO_4)_6O_2$ crystalline phase precipitates in both series after the 800 ℃/120 h heat treatment.

Fig. 8 presents the microstructures of B25 and Mo3 glass samples after heat treatment at 800 °C for 120 h followed by HF etching, as examined by FE-SEM and EDS analysis. Fig. 8a shows the B25 glass containing a high boron oxide concentration

`

of 28.14 wt%. The precipitate in the matrix primarily consists of Ca and Mo, as indicated by EDS mapping. In combination with the XRD results shown in Fig. 3b, the crystalline phase is identified as calcium molybdate ($CaMoO_4$) with a scheelite-type tetragonal structure. The crystals display a highly symmetrical cruciform or flower-like morphology, with an approximate size of 30 μm. Notably, distinct annular etching pits are observed surrounding the precipitates. This feature is directly attributable to the phase-separated structure of the base glass, which gives rise to phases with markedly different resistance to HF etching. Based on the above observations, two types of phase separation are possible in this system: a Na_2O-B_2O_3-rich phase and a Na_2O-MoO_3-rich phase[22,23]. If a Na-Mo-rich phase had formed, it would readily crystallize as Na_2MoO_4 upon heat treatment. However, no Na_2MoO_4 crystals were detected by XRD in the heat-treated glasses (Fig. 3b), and only $CaMoO_4$ was identified as the crystalline phase. This indicates that the presence of Ca^{2+} in the glass composition thermodynamically suppresses the formation of a Na-Mo-rich phase by preferentially binding with molybdate ions to form stable $CaMoO_4$. Therefore, the annular etching pits created by HF treatment are not attributable to a Na-Mo-rich phase; Therefore, the annular etching pits are more plausibly attributed to the selective dissolution of Na_2O–B_2O_3-rich regions rather than Na–Mo-rich domains. ~~instead, they unambiguously correspond to the selective dissolution of the Na_2O-B_2O_3-rich phase~~.The occurrence of etch pits around the $CaMoO_4$ crystals indicates that heterogeneous nucleation preferentially takes place at interfaces of the phase-separated regions, and subsequent crystal growth follows the minimum energy criterion for heterogeneous nucleation. Fig. 8b presents the microstructure of the Mo3 glass sample, in which the molybdenum oxide content of the base glass is 3.44 wt%, after identical heat treatment at 800 °C for 120 h followed by HF etching. Similarly, the Mo3 glass sample precipitates $CaMoO_4$ crystals exhibiting the characteristic cruciform flower-like morphology.

3.6. Competitive Crystallization Mechanism

Fig. 9 presents the Raman spectra of glass samples containing different amounts of B_2O_3. The band near 770 cm^{-1} corresponds to four-coordinated boron in diborate and boroxol rings [24]. In addition, the region between 850 and 950 cm^{-1} represents the primary characteristic domain for the stretching vibration of B–O–Si linkages. The broad band in the 800–1200 cm^{-1} range is closely related to the degree of polymerization of the silicate network, denoted as Q^n species [25]. Here, Q denotes a

silicon-oxygen tetrahedron, and n corresponds to the number of bridging oxygen (BO) atoms. [SiO_4] tetrahedra containing different numbers of bridging oxygens are classified as Q^0, Q^1, Q^2, Q^3, and Q^4 units, with their characteristic Raman bands typically observed at about 840–890 cm^{-1}, 900–950 cm^{-1}, 960–1030 cm^{-1}, 1050–1100 cm^{-1}, and 1160–1190 cm^{-1}, respectively [25].

As shown in Fig. 9, the structure of the glass network evolves progressively with increasing B_2O_3 content in the base composition. The peak at 770 cm^{-1}, which corresponds to four-coordinated boron in diborate and boroxol rings, appears upon increasing B_2O_3 content, indicating that the addition of boron oxide promotes the formation of boroxol ring structures and the generation of four-coordinated boron. The Raman peak located near 915 cm^{-1} cannot be uniquely assigned, as it may correspond either to the stretching vibration of B–O–Si bonds or to Q^1 silicate tetrahedra. Despite this ambiguity, its intensity is observed to decrease monotonically with the addition of B_2O_3. Simultaneously, the peak associated with Q^3 structural units gradually weakens and eventually disappears in the B25 sample.

This structural evolution may be interpreted using the compositional parameter R', defined as the molar ratio of effective alkali oxide (i.e., the total alkali content minus that consumed for charge compensation of $[AlO_4]^-$ tetrahedra) to boron oxide: $R' = ([R_2O] - [Al_2O_3])/[B_2O_3]$. This parameter governs the transformation of $[BO_3]$ units into $[BO_4]$ units and the subsequent generation of non-bridging oxygens (NBOs) [26,27]. The R' value decreases from 2.66 (B5) to 0.42 (B25) across the sample series. When $R' > 0.5$, the addition of B_2O_3 primarily consumes NBOs to form tetrahedrally coordinated $[BO_4]^-$ units, thereby enhancing network polymerization. Theoretically, the fraction of $[BO_4]^-$ units reaches a maximum at $R' = 0.5$, corresponding to the most compact and highly interconnected network structure with the highest concentration of B–O–Si bonds [27]. Accordingly, as R' decreases from 2.66 to 0.42, the observed reduction in the 915 cm^{-1} peak intensity is mainly attributed to the decline in Q^1 unit concentration, which acts as a primary host for NBOs. In the B25 sample containing the highest borate content, the R' value decreases below 0.5, inducing the so-called "boron anomaly" [28]. This phenomenon involves reconversion of boron coordination from four-fold ($[BO_4]$) to three-fold ($[BO_3]$).

`

The observed crystallization behavior, in which the $Ca_2Ln_8(SiO_4)_6O_2$ phase precipitates and its crystallinity decreases from 15% to 0% as the boron oxide content increases from 5 wt% to 15 wt%, followed by the onset of $CaMoO_4$ precipitation (reaching 5% crystallinity at 25 wt% B_2O_3), may be explained by the underlying mechanism described below.

Within the borosilicate glass system, the simultaneous presence of molybdenum (Mo) and rare-earth elements (Ln) results in competition between precipitation of two crystalline phases: scheelite-type calcium molybdate ($CaMoO_4$) and oxyapatite ($Ca_2Ln_8(SiO_4)_6O_2$). Initially, localized chemical environments generated within phase-separated or structurally open regions of the glass matrix serve as reactive sites for nucleation of both phases. Within these microstructural domains, rare-earth ions (Ln^{3+}) and molybdate anions (MoO_4^{2-}) compete for the limited supply of charge-compensating cations, primarily Ca^{2+}, to crystallize, resulting in both thermodynamic and kinetic competition. Trivalent Ln^{3+} ions, owing to their high field strength, polarize the electron cloud of non-bridging oxygens (NBOs) to form negatively charged $[LnO_x]$ coordination complexes that require interstitial Ca^{2+} for charge compensation. In contrast, MoO_4^{2-} anions must capture Ca^{2+} to form neutral crystal units [29]. Direct competition for available Ca^{2+} ions within the glass ultimately determines the crystallization pathway. This mechanism is supported by composition-dependent experimental observations, such as enhanced $CaMoO_4$ precipitation at higher Mo concentrations and promotion of the oxyapatite phase with increased rare-earth oxide content.

Furthermore, intrinsic structural differences between the two crystalline phases reinforce the asymmetric nature of this competition. Formation of one unit cell of $Ca_2Ln_8(SiO_4)_6O_2$ consumes two Ca^{2+} ions, whereas crystallization of one $CaMoO_4$ unit cell requires only one Ca^{2+}. This stoichiometric difference results in distinct crystallization pathways. When the relative CaO content in the glass composition is higher, precipitation of the oxyapatite phase, which requires a greater number of Ca^{2+} ions, becomes kinetically more favorable.

This ionic competition is ultimately governed by the topology of the glass network, in which boron oxide (B_2O_3) plays a crucial regulatory role. In the present borosilicate glass system, B_2O_3 acts as a network former and regulates the concentration and distribution of non-bridging oxygens through boron coordination changes and

`

charge compensation. Specifically, the high field strength of Ln^{3+} ions promotes coordination with NBOs to form localized negatively charged [LnO_x] complexes. These complexes subsequently attract Ca^{2+} cations through electrostatic interactions, providing the thermodynamic driving force for nucleation and growth of the $Ca_2Ln_8(SiO_4)_6O_2$ phase. At elevated NBO concentrations, the abundance of available NBOs enables Ln^{3+} ions to form [LnO_x] complexes with higher local negative charge, thereby conferring a competitive advantage over MoO_4^{2-}. Conversely, as incorporation of B_2O_3 reduces the NBO population, the scarcity of NBOs surrounding Ln^{3+} ions inhibits formation of effective charge-compensating centers. In contrast, the molybdate anion (MoO_4^{2-}) exists as a discrete and structurally stable tetrahedral unit within the glass melt, and its ability to bind Ca^{2+} is largely independent of the ambient NBO concentration. Consequently, addition of B_2O_3, through consumption of NBOs, indirectly weakens the competitive advantage of Ln^{3+}, thereby shifting the crystallization pathway in favor of $CaMoO_4$ formation.

Fig. 10 schematically illustrates how variations in non-bridging oxygen (NBO) concentration determine the preferred crystallization pathway. As previously discussed, for compositions where R > 0.5, progressive addition of boron oxide systematically reduces the NBO concentration within the glass network. This structural modification governs the subsequent phase precipitation process: a higher NBO concentration favors crystallization of the silicate oxyapatite phase $Ca_2Ln_8(SiO_4)_6O_2$, whereas a lower NBO concentration promotes formation of the calcium molybdate ($CaMoO_4$) phase.

4. Conclusions

Simulated waste glasses containing varying proportions of alkaline earth metal oxides, B_2O_3, MoO_3, and rare-earth oxides (RE) were prepared. A systematic examination of the influence of glass components on crystallization behavior yielded the following findings:

The glass composition plays a critical role in determining the crystallization pathway. Incorporation of B_2O_3 and MoO_3 facilitates crystallization of calcium molybdate ($CaMoO_4$) while suppressing precipitation of the oxyapatite phase ($Ca_2Ln_8(SiO_4)_6O_2$). In contrast, addition of alkaline earth metal oxides and rare-earth metal oxides promotes formation of $Ca_2Ln_8(SiO_4)_6O_2$ crystals but inhibits crystallization of $CaMoO_4$. A pronounced competitive relationship exists between

`

precipitation of $CaMoO_4$ and $Ca_2Ln_8(SiO_4)_6O_2$, and optimization of the baseline glass composition can effectively mitigate undesirable crystallization.

The fundamental mechanism governing this composition-dependent competition, particularly the crucial role of B_2O_3, arises from modification of the glass network structure. The principal function of B_2O_3 is regulation of non-bridging oxygen (NBO) concentration. The NBO content determines the competitive balance between high-field-strength Ln^{3+} ions, which form negatively charged $[LnO_x]$ complexes, and structurally independent MoO_4^{2-} anions in their competition for Ca^{2+} cations. By reducing the NBO concentration, incorporation of B_2O_3 indirectly weakens the competitive capability of Ln^{3+}, thereby systematically directing the crystallization pathway from the oxyapatite phase toward calcium molybdate formation.

ACKNOWLEDGMENTS

The authors gratefully appreciate the financial support from the National Natural Science Foundation of China (No. 22576161).

CRediT authorship Contribution Statement

Lejian Zhang: Investigation, Validation, Visualization, Writing – original draft. Ziqiang Jia: Investigation, Writing – review & editing. Jinyang Feng: Supervision, Writing – review & editing. Wei Deng: Supervision, Writing – review & editing. Michael I. Ojovan: Writing – review & editing. Kai Xu: Conceptualization, Methodology, Writing – review & editing, Supervision, Project administration, Funding acquisition.

`

REFERENCES

[1] G. Roth, S. Weisenburger, Vitrification of high-level liquid waste: glass chemistry, process chemistry and process technology, Nucl. Eng. Des. 202 (2000) 197–207.

[2] S. Mandal, G. Suneel, J. Selvakumar, et al., Synthesis and characterization of multi-component borosilicate glass beads for radioactive liquid waste immobilisation, J. Nucl. Mater. 604 (2025) 155485.

[3] S.V. Yudintsev, M.I. Ojovan, V.I. Malkovsky, Thermal Effects and Glass Crystallization in Composite Matrices for Immobilization of the Rare-Earth Element–Minor Actinide Fraction of High-Level Radioactive Waste, J. Compos. Sci. 8 (2) (2024) 70.

[4] M.I. Ojovan, W.E. Lee, Glassy Wasteforms for Nuclear Waste Immobilization, Metall. Mater. Trans. A 42 (4) (2011) 837–851.

[5] K. Xu, Z. Jia, X. Meng, et al., Quantitative assessment of compositional effects on molybdenum solubility in nuclear waste glasses, J. Nucl. Mater. 621 (2026) 156372.

[6] F. Farges, R. Siewert, C.W. Ponader, et al., Structural environments around molybdenum in silicate glasses and melts. II. Effect of temperature, pressure, H_2O, halogens, and sulfur, Can. Mineral. 44 (3) (2006) 755–773.

[7] X. Xu, Y. Yang, S. Kapoor, et al., Structural drivers controlling sulfur solubility in alkali aluminoborosilicate glasses, J. Am. Ceram. Soc. 104 (10) (2021) 5149–5164.

[8]S. Tan, M.I. Ojovan, N.C. Hyatt, et al., MoO_3 incorporation in magnesium aluminosilicate glasses, J. Nucl. Mater. 458 (2015) 335–342.

[9] E. Nicoleau, S. Schuller, F. Angeli, et al., Phase separation and crystallization effects on the structure and durability of molybdenum borosilicate glass, J. Non Cryst. Solids 427 (2015) 120–133.

[10] J.S. McCloy, B.J. Riley, A. Goel, et al., Crystallization study of rare earth and molybdenum containing nuclear waste glass ceramics, J. Am. Ceram. Soc. 102 (9)

`

(2019) 5149–5163.

[11] M.I. Ojovan, J.M. Juoi, A.R. Boccaccini, et al., Glass Composite Materials for Nuclear and Hazardous Waste Immobilisation, MRS Online Proc. Libr. 1107 (1) (2008) 245.

[12] T. Taurines, B. Boizot, et al., Synthesis of powellite-rich glasses for high level waste immobilization, J. Non Cryst. Solids 357 (14) (2011) 2723–2725.

[13] S. H. Tan, J. Chang, J. T. Wang, et al., Phase evolution in dissolution reactions between power reactor high level liquid waste calcines and basic glass, At. Energy Sci. Technol. 59 (1) (2025) 46–56.

[14] R. Jia, C. Niu, X. Liu, et al., Compositional effects on the growth of diopside crystals in the simulated high-level waste glass, J. Am. Ceram. Soc. 107 (12) (2024) 8132–8141.

[15] J. Marcial, J. Crum, et al., Nepheline structural and chemical dependence on melt composition, Am. Mineral. 101 (2) (2016) 266–276.

[16] J. Jiusti, E. Regnier, V. Malivert, et al., Crystallization and rheological study of a Nd-oxyapatite-bearing melt, J. Non Cryst. Solids 628 (2024) 122847.

[17] R. Morena, K. Niihara, D. P. H. Hasselman, Effect of crystallites on surface damage and fracture behavior of a glass-ceramic, J. Am. Ceram. Soc. 66 (10) (1983) 673–682.

[18] P. Frugier, C. Martin, S. Ribet, et al., The effect of composition on the leaching of three nuclear waste glasses: R7T7, AVM and VRZ, J. Nucl. Mater. 346 (2–3) (2005) 194–207.

[19] Z. Jia, C. Liu, C. Niu, K. Li, K. Xu, Volatilization of sodium and boron from nuclear waste glass and associated effects on glass structure and thermal stability, J. Nucl. Mater. 587 (2023) 154712.

[20] K. Maeda, A. Yasumori, Effect of molybdenum and tungsten oxides on nucleation and crystallization behaviors of $MgO–Al_2O_3–SiO_2$ glasses, J. Non-Cryst. Solids 427 (2015) 152–159.

`

[21] A. A. Cabral, J. M. Ferreira, et al., On the determination of the concentration of crystal nuclei in glasses by DSC, J. Am. Ceram. Soc. 96 (9) (2013) 2817–2823.

[22] A. Rafferty, R. G. Hill, D. Wood, An investigation into the amorphous phase separation characteristics of an ionomer glass series and a sodium-boro-silicate glass system, J. Mater. Sci. 38 (2003) 2311–2319.

[23] Y. Zhang, T. Zhang, H. Li, et al., Effect of surface grain structure on reaction of residual glass phase with hydrofluoric acid in glass-ceramics, Ceram. Int. 49 (19) (2023) 32228–32236.

[24] A. A. Osipov, L. M. Osipova, Structure of glasses and melts in the Na_2O-B_2O_3 system from high-temperature Raman spectroscopic data: II. Superstructural units in melts, Glass Phys. Chem. 35 (2) (2009) 131.

[25] P. McMillan, Structural studies of silicate glasses and melts; applications and limitations of Raman spectroscopy, Am. Mineral. 69 (1984) 622–644.

[26] W.J. Dell, P.J. Bray, S.Z. Xiao, ^{11}B NMR studies and structural modeling of Na_2O-B_2O_3-SiO_2 glasses of high soda content, J. Non-Cryst. Solids 58 (1) (1983) 1–16.

[27] Krishnamurthy A, Kumar A. Field strength of network-modifying cation dictates the structure of (Na-Mg) aluminosilicate glasses. Front Mater. 2020;7:267.

[28] M. Wang, Y. Zhang, X. Li, et al., Influence of high-pressure on the short-range structure of Ca or Na aluminoborosilicate glasses from ^{11}B and ^{27}Al solid-state NMR, J. Non-Cryst. Solids 638 (2024) 123085.

[29] N. Chouard, D. Caurant, O. Majérus, et al., Effect of neodymium oxide on the solubility of MoO_3 in an aluminoborosilicate glass, J. Non Cryst. Solids 357 (14) (2011) 2752–2762.

`

Table 1 Nominal compositions of the simulated HLW glasses (wt%)

Series	Sample	MoO_3	REO	AEO	B_2O_3	SiO_2	Al_2O_3	TMO	A_2O	SUM
	CG	2.00	7.00	6.40	14.40	47.90	3.50	6.60	12.20	100.00
Mo	Mo0	**0.00**	7.14	6.53	14.69	48.88	3.57	6.73	12.45	100.00
	Mo1	**1.15**	7.06	6.46	14.52	48.31	3.53	6.66	12.31	100.00
	Mo2（CG）	**2.00**	7.00	6.40	14.40	47.90	3.50	6.60	12.20	100.00
	Mo3	**3.44**	6.90	6.31	14.19	47.19	3.45	6.50	12.02	100.00
	Mo4	**4.58**	6.82	6.23	14.02	46.64	3.41	6.43	11.88	100.00
RE	RE0	2.15	**0.00**	6.88	15.48	51.50	3.76	7.10	13.12	100.00
	RE3	2.08	**3.47**	6.64	14.95	49.72	3.63	6.85	12.66	100.00
	RE6(CG)	2.00	**7.00**	6.40	14.40	47.90	3.50	6.60	12.20	100.00
	RE9	1.93	**10.30**	6.17	13.89	46.20	3.38	6.37	11.77	100.00
	RE12	1.86	**13.66**	5.94	13.37	44.47	3.25	6.13	11.33	100.00
AE	AE5	2.07	7.23	**3.31**	14.87	49.48	3.62	6.82	12.60	100.00
	AE10(CG)	2.00	7.00	**6.40**	14.40	47.90	3.50	6.60	12.20	100.00
	AE15	1.92	6.71	**10.30**	13.80	45.90	3.35	6.32	11.69	100.00
B	B5	2.20	7.70	7.04	**5.82**	52.70	3.85	7.26	13.42	100.00
	B10	2.07	7.23	6.61	**11.54**	49.50	3.62	6.82	12.61	100.00
	B15(CG)	2.00	7.00	6.40	**14.40**	47.90	3.50	6.60	12.20	100.00
	B20	1.81	6.32	5.78	**22.70**	43.26	3.16	5.96	11.02	100.00
	B25	1.68	5.88	5.37	**28.14**	40.21	2.94	5.54	10.24	100.00

REO includes La_2O_3, CeO_2, and Nd_2O_3; AEO includes CaO and BaO; TMO includes ZnO, ZrO_2, and Fe_2O_3; and A_2O includes to Na_2O and Li_2O.

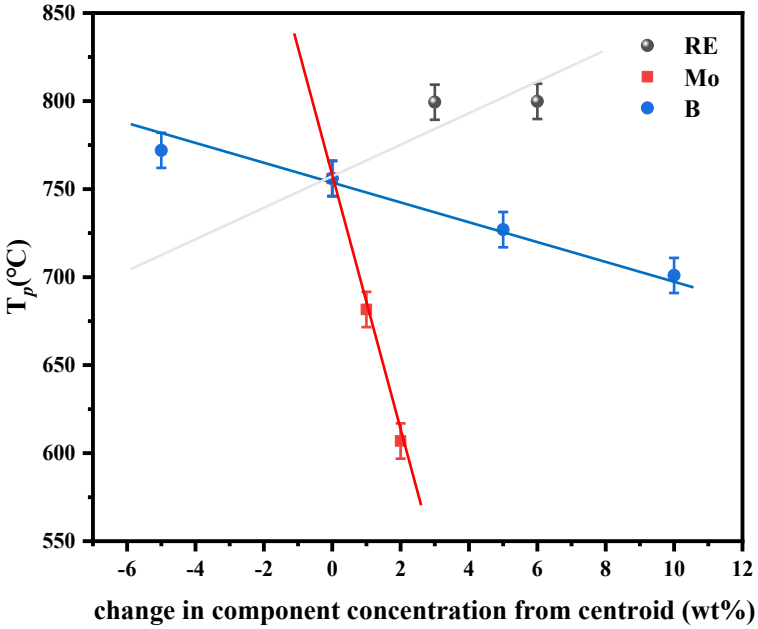

Fig. 1. Dependence of crystallization peak temperature (T_p) on composition for various glass compositions.

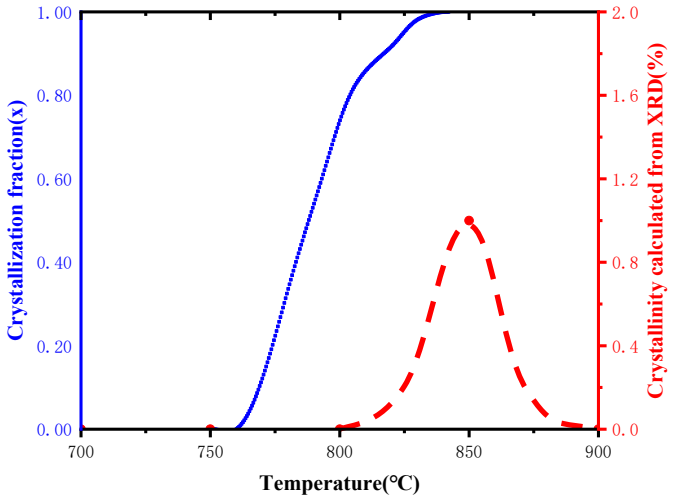

Fig. 2. Dependence of crystallization fraction (derived from DSC) and crystallinity (obtained from semi-quantitative XRD analysis) of CG glass sample on heat-treatment temperature.

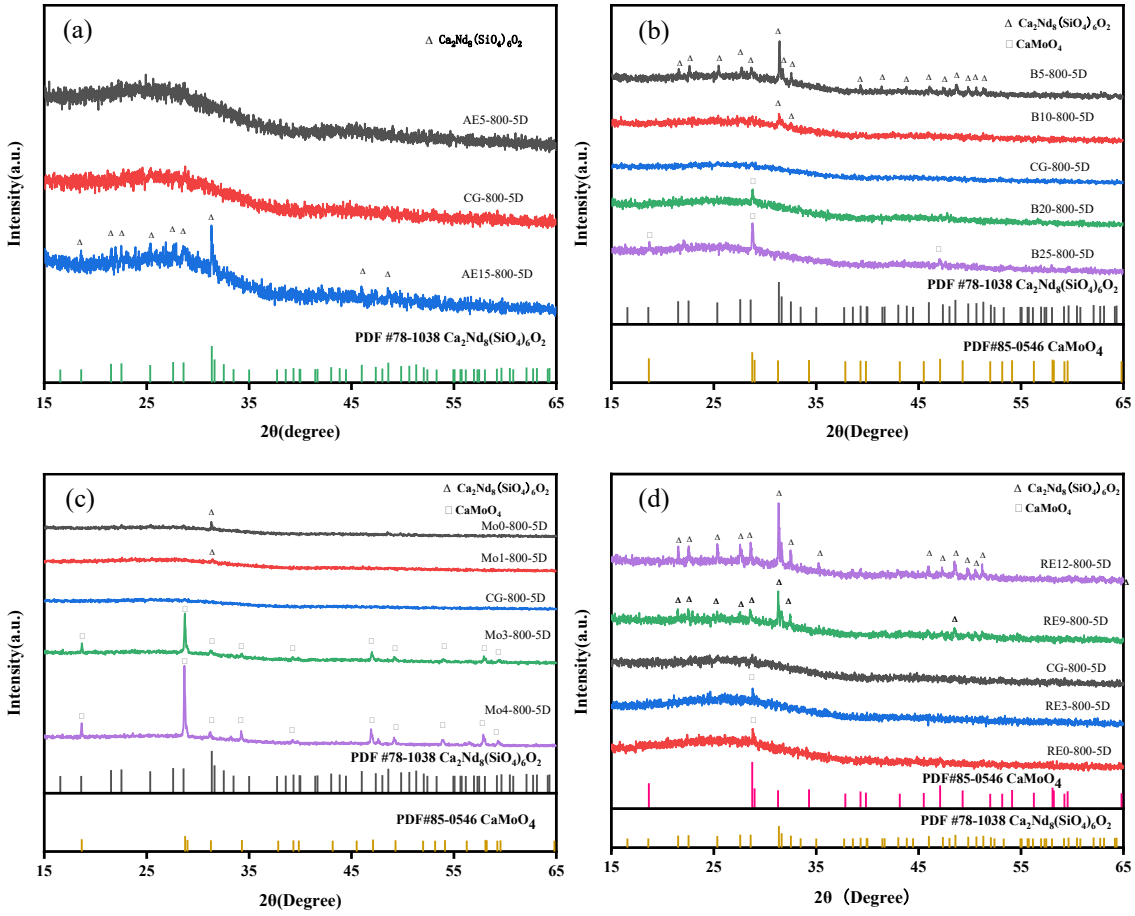

Fig. 3. XRD patterns of different compositional glass samples heat-treated at 800 °C for 120 h: (a) series with varying alkaline earth oxide content; (b) series with different boron oxide (B_2O_3) contents; (c) series with different molybdenum oxide content; (d) series with different rare-earth oxide contents.

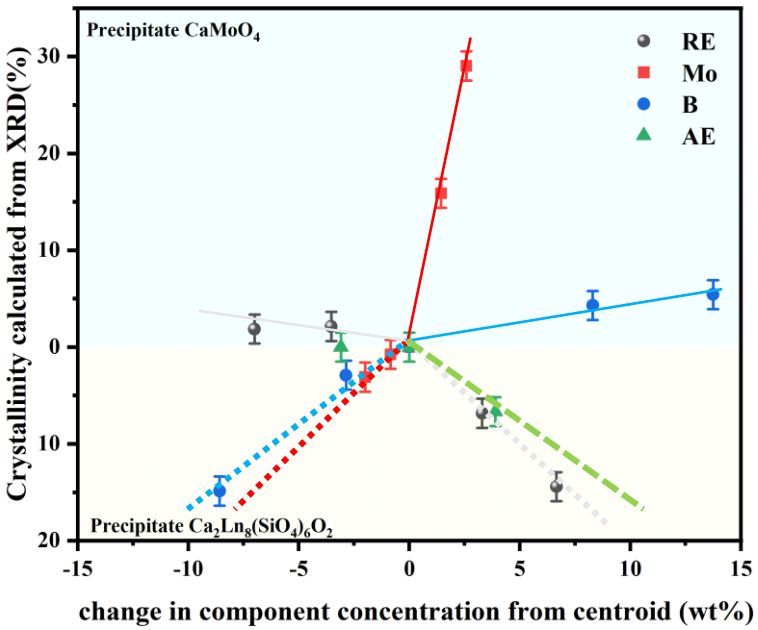

Fig. 4. Spider diagram of crystallinity variation with different compositional glass samples heat-treated at 800 °C for 120 h.

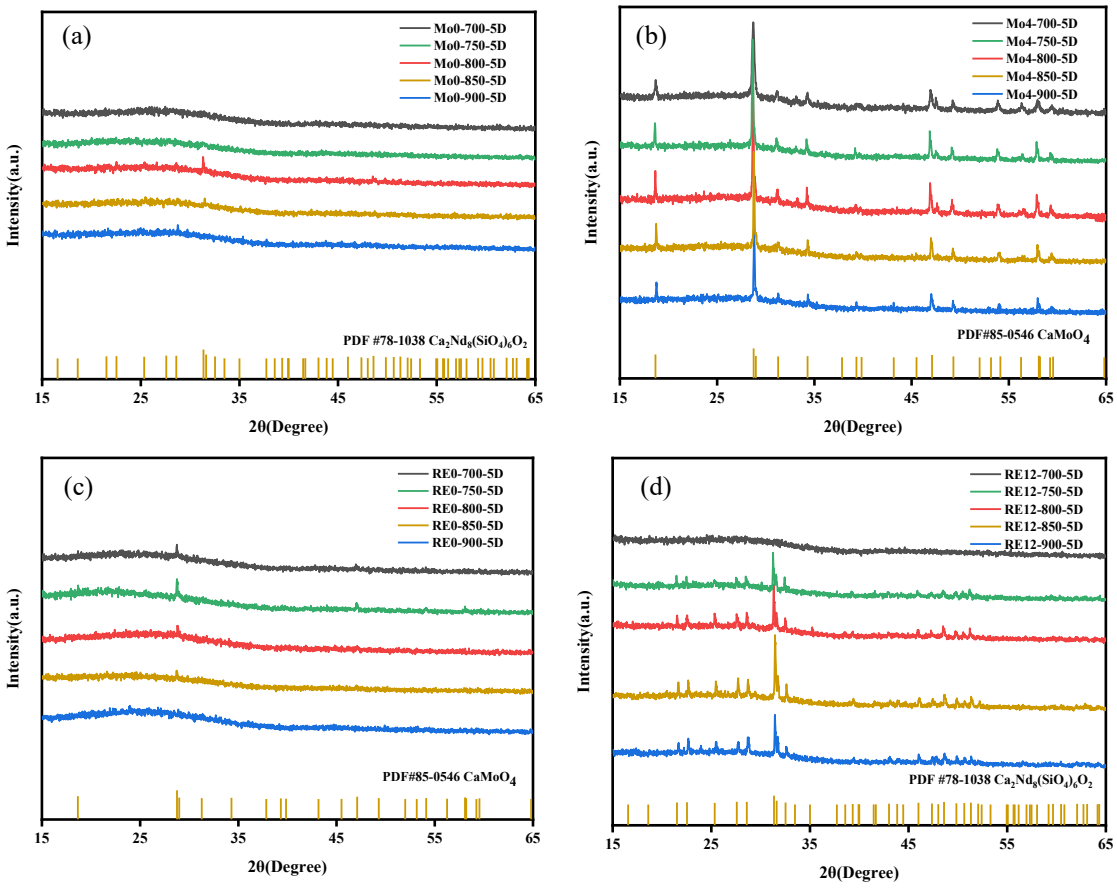

Fig. 5. XRD patterns of different glass samples heat-treated at different temperatures for 120 h: (a) Mo0 glass, (b) Mo4 glass, (c) RE0 glass, and (d) RE12 glass.

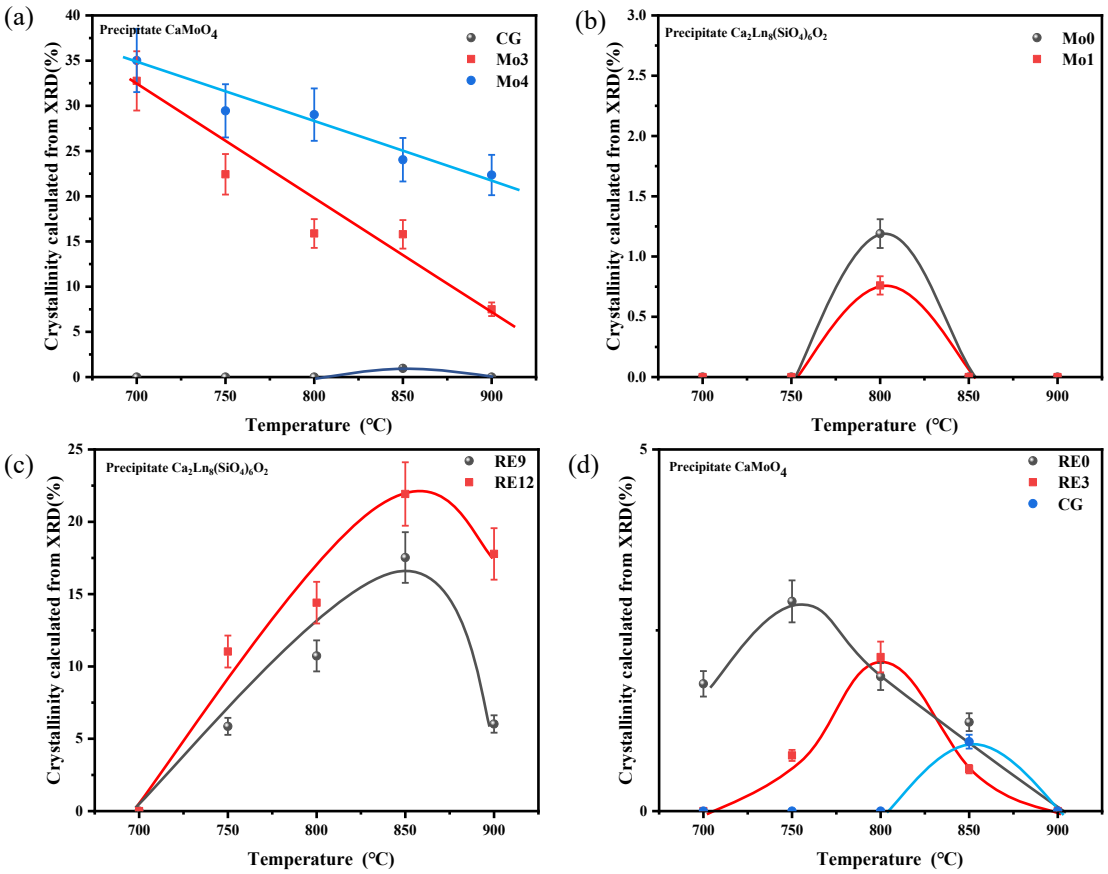

Fig. 6. Crystallinity of different glasses as functions of heat-treatment temperature (duration: 120 h): (a) high-Mo content and CG glasses, (b) low-Mo content glasses, (c) high-RE content glasses, and (d) low-RE content and CG glasses.

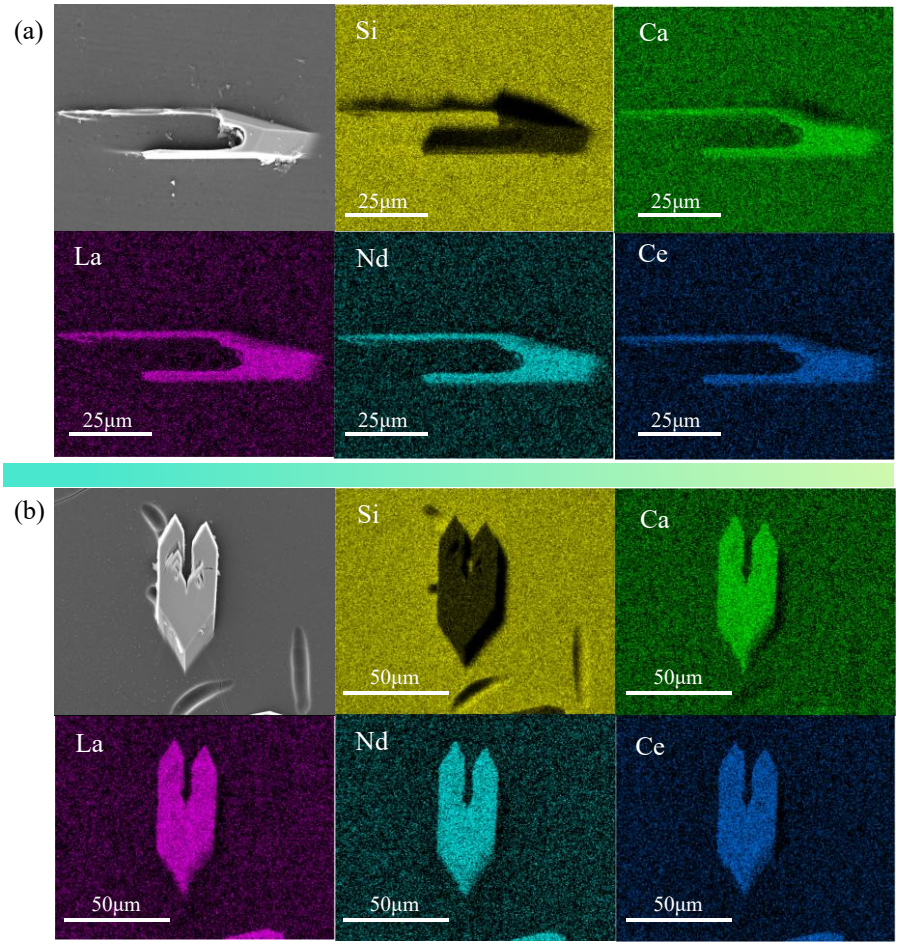

Fig. 7. SEM image and EDS elemental mapping of (a) B5 and (b) RE12 glasses heat-treated at 800 °C for 120 h.

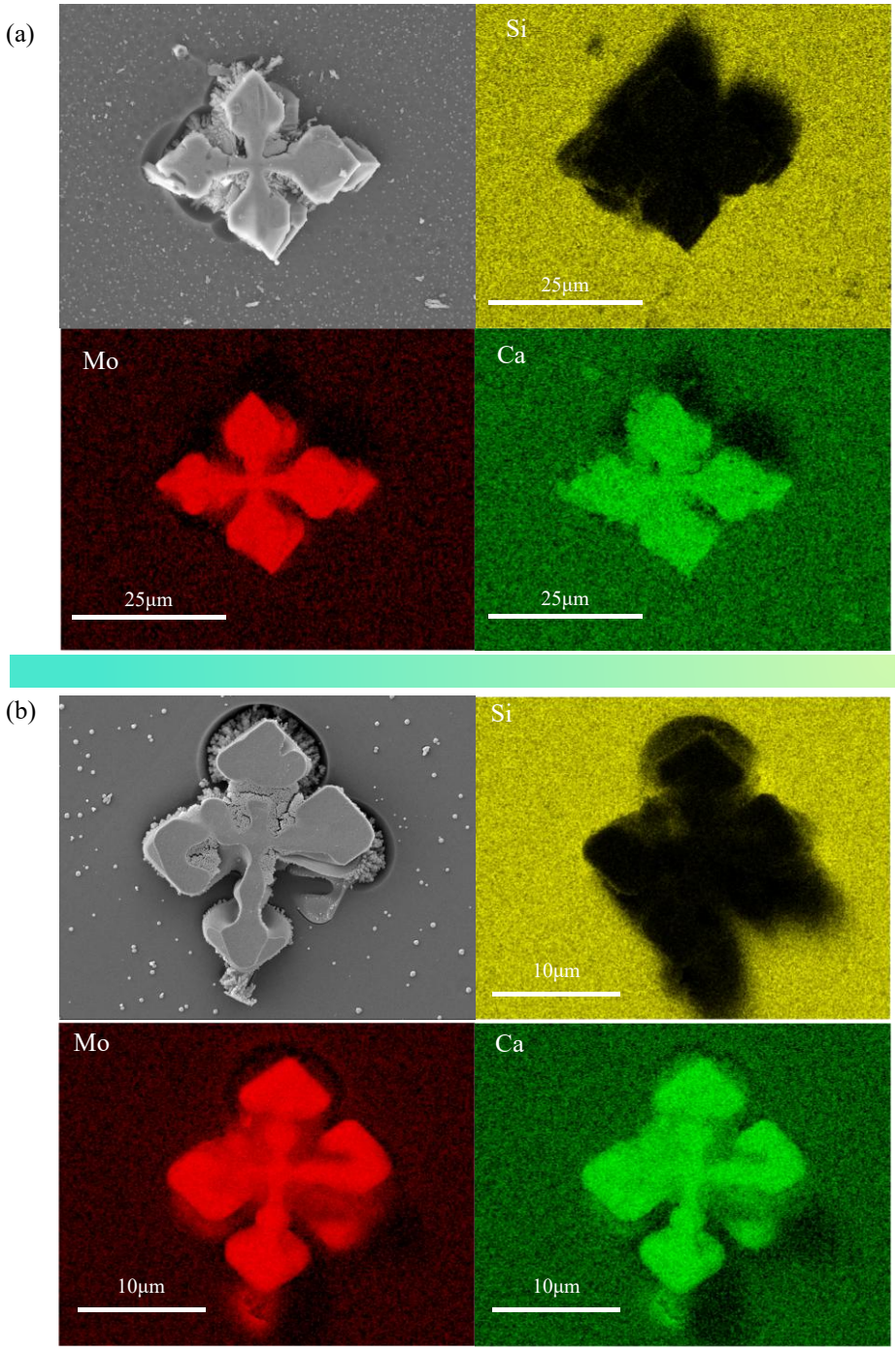

Fig. 8. SEM image and EDS elemental mapping of (a) B25 and (b)Mo3 glasses heat-treated at 800 °C for 120 h.

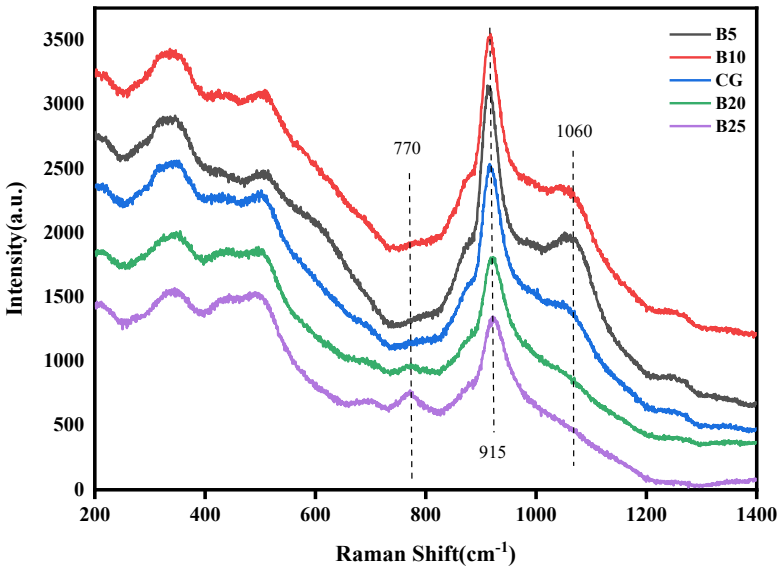

Fig. 9. Raman spectra of glass samples with varying B_2O_3 concentrations.

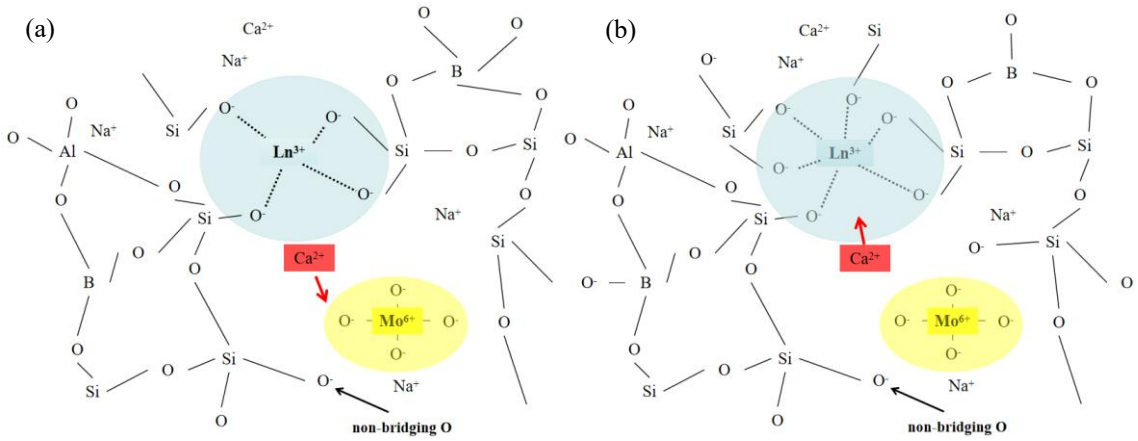

Fig. 10. Schematic representation of the competitive crystallization mechanism regulated by NBO concentration: (a) precipitation of $CaMoO_4$ favored at low NBO levels; (b) precipitation of $Ca_2Ln_8(SiO_4)_6O_2$ favored at high NBO levels.